Molecular and biochemical insights into dysregulation of glycosphingolipid metabolism in a mouse model of Lysosomal Free Sialic Acid Storage Disorder

Marya S. Sabir[1,2], Mahin S. Hossain[3], Laura Pollard[4], Petcharat Leoyklang[3], Marjan Huizing[3], William A. Gahl[1,3], Frances M. Platt[5,§], and May Christine V. Malicdan[1,3,§]

[1]UDP Translational Laboratory, NIH Undiagnosed Diseases Program, National Human Genome Research Institute, National Institutes of Health, Bethesda, MD, USA

[2]NIH Oxford-Cambridge Scholars Program, University of Oxford, Oxford, UK

[3]Human Biochemical Genetics Section, Medical Genetics Branch, National Human Genome Research Institute, National Institutes of Health, Bethesda, MD, USA

[4]Biochemical Genetics Laboratory, Greenwood Genetic Center, Greenwood, SC, USA

[5]Department of Pharmacology, University of Oxford, Oxford, UK

[§]Frances M. Platt and May Christine V. Malicdan are joint senior authors

*Address correspondence to:

- Frances Platt, PhD, FRS, FMedSci: Department of Pharmacology, University of Oxford, Mansfield Road, Oxford OX1 3QT, UK; frances.platt@pharm.ox.ac.uk
- May Christine V. Malicdan, MD, PhD: 10 Center Drive - MSC 1851 Building 10, Room 10C103 Bethesda, Maryland 20892-1851, USA; maychristine.malicdan@nih.gov

Abstract

Free sialic acid storage disorder (FSASD) is caused by pathogenic variants in *SLC17A5*, which encodes the lysosomal sialic acid exporter, sialin. FSASD is characterized by the accumulation of lysosomal free sialic acid, leading to either a severe, childhood-lethal form or a more slowly progressive neurodegenerative disorder associated with the p.Arg39Cys (p.R39C) variant, i.e., Salla disease. While dysregulated glycosphingolipid (GSL) metabolism has been observed in cellular models of FSASD, this study provides the first *in vivo* biochemical dissection of GSL metabolism in a knock-in mouse model harboring the *Slc17a5* p.R39C variant. We employed an integrated multi-modal approach, including sialic acid quantification, exploratory untargeted lipidomics, HPLC-based GSL profiling, bulk transcriptomics, and 4-MU-based lysosomal enzyme activity assays in brain and peripheral tissues (liver and kidney). Exploratory untargeted lipidomic screening revealed region-dependent lipid alterations, with more pronounced changes in the cerebellum than in the forebrain. Pathway-level analyses indicated enrichment of lipid classes related to sphingolipid and GSL metabolism. Targeted biochemical analyses demonstrated that several GSL species accumulate predominantly in the brain, with minimal changes in peripheral tissues, whereas glucosylceramide levels were significantly reduced in all brain regions analyzed. Transcriptomic profiling identified dysregulation of several genes involved in GSL and sialic acid metabolism. Enzyme activity assays corroborated the transcriptomic findings, demonstrating increased activity of several lysosomal glycohydrolases, including neuraminidase 1/3/4 and β-hexosaminidase. Collectively, these findings highlight dysregulated GSL metabolism as a prominent biochemical consequence of sialin deficiency *in vivo* and highlight its putative role in FSASD neuropathology.

Word count: 242/250

Keywords (up to 7): Salla disease; SLC17A5; sialin; glycosphingolipids; gangliosides; neuraminidase; neurodegeneration

Highlights

- Dysregulation of glycosphingolipid (GSL) metabolism in FSASD remains poorly defined
- Slc17a5-R39C/R39C mice show elevated free sialic acid levels in multiple tissues
- Slc17a5-R39C/R39C mice accumulate GSLs, but exhibit reduced glucosylceramide levels
- Slc17a5-R39C/R39C mice display increased activity of several GSL catabolic enzymes
- Altered GSL metabolism is a key biochemical defect in FSASD, especially in the brain

Graphical abstract

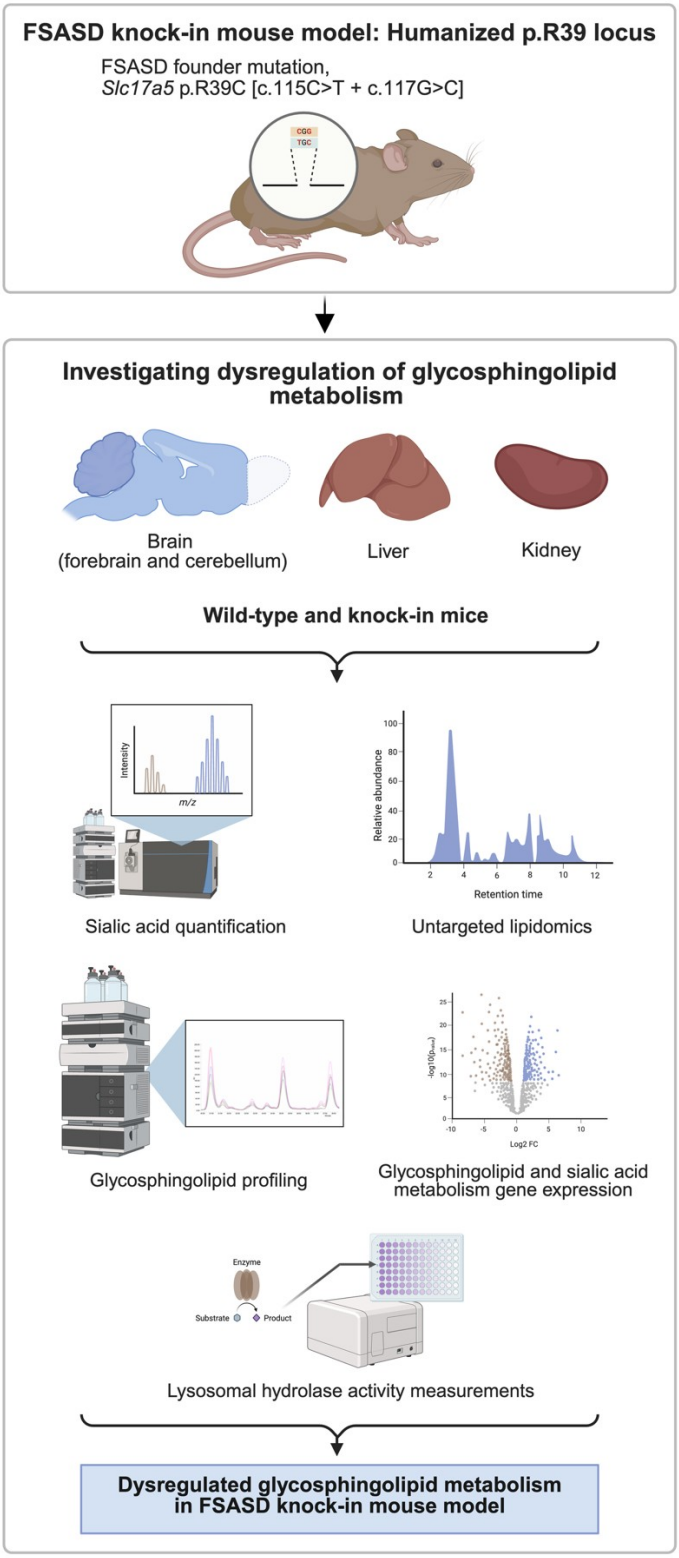

FSASD, free sialic acid storage disorder. Figure created using BioRender.com.

Introduction

Lysosomal free sialic acid storage disorder (FSASD) is an ultra-rare, neurodegenerative disease caused by biallelic loss-of-function variants in *SLC17A5*, which encodes sialin, a lysosomal membrane transporter responsible for the efflux of sialic acid and other acidic hexoses from the lysosome to the cytosol (Aula et al., 1979; Blom et al., 1990; Courville et al., 2010; Mancini et al., 1991; Morin et al., 2004; Pietrancosta et al., 2012; Renlund et al., 1983; Verheijen et al., 1999). Loss of sialin function result in the accumulation of unconjugated ("free") sialic acid in lysosomes within cells of multiple tissues, including the brain (Morin et al., 2004; Sagne and Gasnier, 2008; Wreden et al., 2005). Clinically, FSASD encompasses a spectrum ranging from infantile sialic acid storage disease (MIM#269920), which is often fatal in early childhood, to Salla disease (MIM#604369), a milder, slowly progressive neurodegenerative disorder with survival into late adulthood (Adams and Wasserstein, 2020; Aula et al., 1979; Huizing et al., 2021; Renlund et al., 1983; Verheijen et al., 1999). To date, approximately 250 cases of FSASD have been reported worldwide, with >75% of cases carrying the common missense variant, *SLC17A5* c.115C>T (p.Arg39Cys; p.R39C) typically associated with Salla disease (Aula et al., 2000; Huizing et al., 2021). Neurological features include mild-to-moderate psychomotor delay, spasticity, athetosis, seizures, cognitive impairment, and progressive ataxia (Adams and Wasserstein, 2020; Huizing et al., 2021), and neuroimaging commonly shows hypomyelination, corpus callosum hypoplasia, and progressive cerebellar atrophy (Barmherzig et al., 2017; Haataja et al., 1994; Huizing et al., 2021; Kleta et al., 2004; Morse et al., 2005; Sonninen et al., 1999).

Although free sialic acid accumulation is the defining biochemical hallmark of FSASD, it likely does not fully account for the severity and complexity of the neurological phenotype. FSASD belongs to a wider group of lysosomal storage disorders (LSDs), including GM1 and GM2 gangliosidoses, Gaucher disease, and Niemann-Pick disease, many of which exhibit disruptions in glycosphingolipid (GSL) metabolism, a pathway essential for neuronal differentiation (Rosner, 2003) and synaptic function (Svennerholm, 1980). Gangliosides, the predominant sialylated GSLs in the brain (Schnaar et al., 2009), bind myelin-associated

glycoproteins and contribute to myelin stability and axon structure (Vyas and Schnaar, 2001; Yang et al., 1996). Given that sialic acid salvage/recycling is disrupted in FSASD (Gilormini et al., 2016) and prior studies have shown impaired turnover of sialoglycoproteins and gangliosides in patient fibroblasts (Chigorno et al., 1996; Pitto et al., 1996) and iPSC-derived neural cell types (Sabir et al., 2025a), together with elevated cerebrospinal-fluid gangliosides in FSASD (Sabir et al., 2025b), we hypothesized that GSL metabolism is perturbed *in vivo* and may contribute to FSASD neuropathology. The regulation of GSL metabolism in *in vivo* FSASD models remains poorly defined, despite its role as a convergent pathogenic mechanism across several LSDs. Moreover, it is unknown whether GSL abnormalities are primary consequences of impaired lysosomal sialic acid handling (e.g., sialidase inhibition, lysosomal microenvironment changes) or secondary sequelae of progressive neurodegeneration and cell loss, and whether lysosomal catabolic responses are engaged sufficiently. This gap constrains mechanistic understanding and hinders informed selection of therapeutic targets for FSASD.

Here, using a knock-in mouse model harboring the *Slc17a5* p.R39C variant, we combine complementary biochemical and multi-omic approaches, including sialic acid quantification, untargeted lipidomics, HPLC-based GSL profiling, transcriptomic analyses, and lysosomal enzyme activity assays to profile GSL homeostasis across central (forebrain and cerebellum) and peripheral (liver and kidney) tissues. These analyses reveal widespread GSL dysregulation, highlight region-specific vulnerabilities, and provide mechanistic insights into FSASD-associated neuropathology.

Materials and Methods

Description of mouse model

For this study, we utilized a Slc17a5-R39C/R39C (*Slc17a5* knock-in; knock-in) mouse model harboring the human-equivalent *SLC17A5* p.R39C variant. Using CRISPR-Cas12a, we introduced two nucleotide alterations (c.115C>T and c.117G>C) into exon 2 of the murine *Slc17a5* gene (NM_172773), thereby humanizing the sequence to generate the p.R39C variant in mice in the C57BL/6J-129S1/SvlmJ hybrid background (*manuscript under review*; (Sabir et al., 2022)). Briefly, knock-in mice exhibit notable phenotypic differences by three weeks of age, including reduced body size compared to wild-type littermates, as well as the onset of neurological impairments such as tremors, ataxia, and seizures. By 1.5 months of age, 25% of homozygous mice experienced severe disease progression, with nearly 50% mortality by six months, primarily due to the progression of ataxia and hindlimb paralysis.

Detailed information on the experimental mouse cohorts used in each study arm is available in Supplementary Table 1. All analyses were conducted using independent biological replicates from the cohorts described.

Quantitative analysis of sialic acid levels

Mice (n = 3 wild-type and n = 3 Slc17a5-R39C/R39C; detailed in Supplementary Table 1, Cohort I) were perfused with phosphate-buffered saline (PBS) prior to tissue collection. Isolated tissues were flash-frozen in liquid nitrogen, transferred to dry ice, and stored at -80°C. Brain (right forebrain, right cerebellum), liver, and kidney were collected. Tissues were homogenized in water to achieve a final concentration of 25 mg wet tissue per mL. Frozen homogenates were subsequently shipped to Greenwood Genetic Center (Greenwood, SC, USA) for quantification of free and total sialic acid levels (see Supplementary Materials and Methods). Each measurement represents an independent biological replicate. Neu5Ac, the most abundant sialic acid in mammalian brains (Davies and Varki, 2015; Schauer and Kamerling, 2018), was measured and is referred to as “sialic acid” in this manuscript.

Untargeted lipidomics studies

Mouse tissues from n = 2 wild-type and n = 2 Slc17a5-R39C/R39C mice (detailed in Supplementary Table 1, Cohort II) were isolated, flash-frozen in liquid nitrogen, and placed on dry ice before being stored at -80°C. The following regions were collected: left hemisphere (excluding the olfactory bulb, including the brainstem); right forebrain; and right cerebellum. Samples were then shipped to Creative Proteomics (Shirley, NY, USA) for untargeted lipidomics (see Supplementary Materials and Methods). Each measurement represents an independent biological replicate.

Raw data acquired in both ESI- (negative ion mode) and ESI+ (positive ion mode) were processed and aligned using LipidSearch software (Thermo) based on mass-to-charge (m/z) values and retention times. The aligned peak tables provided by Creative Proteomics were imported into R (version 4.3.0) for downstream analyses. Data quality control, normalization, and subsequent analyses were performed using the lipidR package (version 2.13.0, (Mohamed et al., 2020)). Signal intensities were normalized using probabilistic quotient normalization (PQN) as implemented in the lipidR package (Dieterle et al., 2006; Mohamed et al., 2020). PQN compares the distribution of intensity quotients between each sample and a reference spectrum derived from the dataset and corrects for dilution-related and systematic technical variation by estimating a sample-specific dilution factor used to scale the data. Following normalization, multivariate and univariate analyses were conducted, including principal component analysis (PCA), hierarchical clustering, differential lipid abundance, and lipid class enrichment analyses. Pathway-level analyses were performed using the LipidSig web interface (Lin et al., 2021).

Note, monohexosylceramides detected in the untargeted lipidomics dataset are reported as Hex1Cer species, as reversed-phase LC-MS does not allow unambiguous discrimination between glucosylceramide (GlcCer) and galactosylceramide (GalCer).

Quantification of glycosphingolipids (GSLs) via HPLC

Mice from Cohorts I (n = 3 wild-type and n = 3 Slc17a5-R39C/R39C) and III (n = 4-5 wild-type and n = 3-6 Slc17a5-R39C/R39C; detailed in Supplementary Table 1) were perfused with PBS prior to tissue collection. Brain (right forebrain and right cerebellum), liver, and kidney were isolated, flash-frozen in liquid nitrogen, transferred to dry ice, and stored at -80 °C until further analysis.

Tissues were homogenized in water to achieve a final concentration of 25 mg wet tissue per mL. GSL profiling of mouse tissue homogenates was performed using published methods (Priestman et al., 2024). Briefly, lipids were extracted overnight at 4°C using a chloroform-methanol solution. GSLs were then isolated through solid-phase extraction using C18 columns (Telos). Following elution, the GSL fractions were evaporated under nitrogen at 42°C, then digested with recombinant ceramide glycanase (rEGCase, synthesized by Genscript) to cleave oligosaccharides from complex GSLs or Cerezyme® (Genzyme) to hydrolyze GlcCer and release glucose. The released glycans/glucose were fluorescently labeled with anthranilic acid (2AA), and excess labeling reagent was removed using DPA-6S SPE columns (Supelco). The purified 2AA-labeled oligosaccharides/glucose were analyzed and quantified by normal-phase high-performance liquid chromatography (HPLC). A 2AA-labeled glucose homopolymer ladder (Ludger Ltd) was used to assign glucose unit (GU) values to the HPLC peaks. Specific GSL species were identified by their corresponding GU values (see Fig. S5) and quantified by comparing the integrated peak areas to a known 2AA-labeled BioQuant chitotriose standard (Ludger Ltd). The data were normalized to total protein content, which was determined using the bicinchoninic acid (BCA) assay per standard procedures. Each measurement represents an independent biological replicate.

Total GSLs were determined by rEGCase-mediated digestion of complex GSLs not including monohexosylceramides. Targeted quantification of GlcCer was performed separately using normal-phase HPLC following Cerezyme (glucocerberosidase)-mediated digestion of GSLs, which selectively hydrolyzes GlcCer and does not detect GalCer. All GlcCer values reported in this study derive from this separate targeted assay.

Details of sialic acid measurement of 2AA-labeled GSLs are provided in the Supplementary Materials and Methods.

Immunofluorescence studies

Immunofluorescence studies were performed as described in the Supplementary Materials and Methods.

Bulk transcriptomics studies

Wild-type (n = 4) and Slc17a5-R39C/R39C (n = 4) mice (detailed in Supplementary Table 1, Cohort IV) were perfused with PBS, and brain (right forebrain, right cerebellum) tissues were subsequently isolated and flash-frozen in liquid nitrogen before being placed on dry ice and stored at -80°C. Samples were then shipped to Azenta Life Sciences Inc. (South Plainfield, NJ, USA) for bulk RNA sequencing (see Supplementary Materials and Methods). Each measurement represents an independent biological replicate.

Reads were aligned to the *Mus musculus* reference genome (GRCm38) using HISAT2 (Kim et al., 2019), and read counts were obtained with the DESeq2 R package (version 1.41.2) (Love et al., 2014). Genes involved in GSL metabolism, including biosynthesis and catabolism pathways previously compiled (Platt, 2023) were examined. Sialic acid metabolism genes were curated from the literature (Saeui et al., 2018). Volcano plots were generated using the EnhancedVolcano R package (version 1.19.0) (Blighe, 2018). All quality control and downstream analyses were performed using R (version 4.3.0).

Measurement of lysosomal glycohydrolase activities

Tissues from mice detailed in Supplementary Table 1 (Cohort I; n = 3 wild-type and n = 3 Slc17a5-R39C/R39C) were collected and processed as described in the "Quantification of glycosphingolipids (GSLs)" section above.

Lysosomal glycohydrolase activities in tissue homogenates were measured fluorometrically using synthetic sugar substrates conjugated to the fluorophore 4-methylumbelliferone (4-MU), following established protocols (Huebecker et al., 2019). Neuraminidase (Neu) activity was assessed using two separate assays, i.e., one to quantify Neu1/3/4 activity and another to measure cytosolic Neu2. Both assays utilized 4-MU N-acetylneuraminic acid, with incubations performed for 4 hr (brain) and 1 hr (liver and kidney) at 37°C. Total β-hexosaminidase and HexA activities were measured using 4-MU N-acetyl-β-D-glucosaminide and incubated for 30 min across all tissues at 37°C. Gba1 and Gba2 activities were assessed using 4-MU β-D-glucoside, with incubation for 30 min at 37°C, except for Gba2 activity in the brain, which was incubated for 3 hr. N-butyldeoxygalactonojirimycin was used to selectively inhibit Gba2 activity, enabling the determination of Gba1 activity levels (Ridley et al., 2013). β-galactosidase and α-galactosidase activities were evaluated using 4-MU β-D-galactopyranoside and 4-MU α-D-galactoside, respectively, with a 30 min incubation at 37°C. α-glucosidase and α-mannosidase activities were measured using 4-MU α-D-glucopyranoside and 4-MU α-D-mannopyranoside, respectively, with a 30 min incubation at 37°C, except for α-mannosidase activity in the brain, which was incubated for 3 hr. All reactions were terminated with cold 0.5 M Na_2CO_3 (pH 10.7), and the released fluorescent 4-MU was quantified using a FLUOstar OPTIMA plate reader (BMG Labtech) with excitation at 360 nm and emission at 450 nm. Enzyme activities were calculated from a standard curve of unconjugated 4-MU and normalized to protein content, as determined by the BCA assay. Each measurement represents an independent biological replicate.

Cholesterol abundance studies

Mouse tissues (n = 3 wild-type and n = 3 Slc17a5-R39C/R39C; detailed in Supplementary Table 1, Cohort I) were collected and processed as described in the “Quantification of glycosphingolipids (GSLs)” section above. Cholesterol abundance was quantified as detailed in the Supplementary Materials and Methods. Each measurement represents an independent biological replicate.

Statistical methods

Statistical analyses were conducted using an unpaired t-test or ordinary ANOVA with Šídák's multiple comparisons test using GraphPad Prism (GraphPad, version 10.0.3). A two-tailed α-value for significance was set at 0.05.

Results

Free sialic acid levels are elevated in mouse central and peripheral tissues

Using UPLC-MS/MS, we quantified free and total sialic acid levels in forebrain, cerebellum, liver, and kidney (Cohort I; n = 3 mice per genotype). Compared to wild-type mice, knock-in mice exhibited significant increases in free sialic acid: 9.5-fold (forebrain), 19.5-fold (cerebellum), 42.4-fold (liver), and 17-fold (kidney) (Fig. 1A). Total sialic acid levels were also higher in the knock-in mouse forebrain (1.4-fold), cerebellum (1.7-fold), and liver (13.1-fold) compared to wild-type mice (Fig. 1B) with an upward trend in the kidney (Fig. 1B). Bound sialic acid levels, calculated by subtracting free from total sialic acid levels, were increased only 3.9-fold in the liver (Fig. 1C). These results confirm the canonical FSASD biochemical defect across all mouse tissues examined. Given this indication of metabolic disruption, we next examined whether global lipid networks were correspondingly altered.

Exploratory untargeted lipidomics suggests brain region-specific vulnerability in knock-in mice

We performed exploratory untargeted lipidomic analyses using UPLC-MS in both positive and negative ion modes on right cerebellum, right forebrain, and left hemisphere samples (Cohort II; n = 2 mice per genotype). Following normalization and multivariate analyses (Fig. S1), lipid profiles suggested region-dependent differences, with more extensive alterations observed in the cerebellum compared to the forebrain and hemisphere (Figs. S2A and S2B). Lipid class enrichment analyses also revealed distinct regional signatures. In the positive ion mode, multiple lipid classes were enriched in the cerebellum and forebrain, whereas enrichment in the hemisphere was limited and primarily driven by monohexosylceramides (Hex1Cer; Fig. S2C). In the negative ion mode, enriched lipid classes were

detected predominantly in the cerebellum and hemisphere, with no enrichment observed in the forebrain (Fig. S2D). Region-agnostic analyses highlighted Hex1Cer across both ionization modes and ceramides (Cer) in the negative ion mode (Figs. S3A and S3B). Pathway-level mapping using Reactome suggested involvement of sphingolipid-related pathways, including GSL metabolism (Figs. S3C and S3D). These findings were used to guide subsequent targeted biochemical analyses.

GSLs are primarily altered in the knock-in mouse brain

Because Hex1Cer species were among the most altered lipid classes, we quantified GSLs using two orthogonal normal-phase HPLC assays in forebrain, cerebellum, liver, and kidney (Cohort I; n = 3 mice per genotype). Compared to wild-type mice, the knock-in mice displayed significantly altered GSL levels, primarily in the cerebellum, with modest changes observed in the forebrain. In the forebrain, GM2 and GA1 levels were significantly elevated, while total GSLs and most other detected species showed non-significant upward trends (Figs. 2A, S4A, and S4B). In contrast, the cerebellum exhibited a marked increase, with total GSL levels and nearly all detected species showing significant elevations relative to wild-type mice (Figs. 2B, S4A, and S4B). Notably, glucosylceramide (GlcCer) levels were significantly reduced in both the forebrain and cerebellum of knock-in mice (Figs. 2A and 2B).

Peripheral tissues exhibited more modest changes. The liver displayed increases in GM3 and Gb3 with no other significant differences (Figs. 3A, S4A, and S4B), although GlcCer showed a downward trend (Fig. 3A). The kidney showed no marked changes, with Gb4 levels trending upward (Figs. 3B, S4A, S4B, and S4C). Refer to Figure 7A for a summary of the GSL results across all examined tissues, and Supplementary Figure 5 for representative GSL HPLC traces from the mouse forebrain, cerebellum, liver, and kidney, along with GlcCer in the brain (similar singular peak for all tissues).

To validate our findings from Cohort I in a larger cohort while controlling for biological sex, we performed GSL analyses in both the forebrain and cerebellum at three timepoints, i.e., 21 days,

approximately 3 months, and approximately 5 months in Cohort III (n = 4-5 wild-type and n = 3-6 Slc17a5-R39C/R39C male mice). In the forebrain, at approximately 5 months of age, knock-in mice exhibited a trend toward increases in total GSLs and in all detected species, except for GlcCer (Fig. S6). Notably, GM2 and GA1 were elevated, while GlcCer levels were consistently decreased across all timepoints by approximately 24-fold, 32-fold, and 13-fold at 21 days, ~3 months, and ~5 months, respectively (Fig. S6). In the cerebellum, fewer overall changes were observed, although several GSL species showed upward trends, while GlcCer levels were consistently decreased—by approximately 3.5-fold, 3.1-fold, and 1.7-fold at 21 days, ~3 months, and ~5 months, respectively (Fig. S7). Specifically, GM2 levels were significantly elevated at 21 days, and GA1 showed an increase at all timepoints (Fig. S7). Collectively, these findings suggest significant alterations in GSL abundance in the brain, particularly a pronounced accumulation in species excluding GlcCer. Moreover, some region-specific alterations may reflect sex-based differences, as Cohort I consisted predominantly of females, while Cohort III included only males.

Given the consistent elevation of GM2 in the forebrain and cerebellum of mice from both Cohort I and Cohort III, we performed immunofluorescence studies to examine GM2 expression in male mice at approximately 3 months (91 days) and nearly 9 months (270 days) of age (n = 1 mouse per genotype per timepoint). Although GM2 accumulation was detected biochemically in both forebrain and cerebellum, imaging was focused on regions showing the most pronounced differences between genotypes. As confirmed by a survey of the entire brain, GM2 accumulation was localized predominantly to the cerebellum and pons, where staining was more prominent in knock-in compared with wild-type mice at both timepoints (Fig. S8). At 270 days, colocalization of GM2 with the lysosomal marker LAMP1 was more apparent in the pons than in the cerebellum, although overlap was also observed in the cerebellum (Figs. S8B and S8D). Notably, LAMP1 staining was increased in the knock-in mouse brain (Fig. S8), which could indicate lysosomal accumulation and/or enlargement.

Exploratory analyses quantifying sialic acid derived from 2AA-labelled GSLs in mouse brain tissue (from Fig. 2, Cohort I; n = 3 mice per genotype) revealed a significant elevation of sialic acid in the cerebellum, but not in the forebrain (Fig. S9). This observation likely corresponds to the increase in total GSLs observed in the cerebellum, but not in the forebrain (Figs. 2A and 2B). Furthermore, given that both cholesterol and GSLs are critical components of lipid rafts in the plasma membrane (Simons and Ikonen, 1997), we assessed cholesterol levels in brain homogenates from Cohort I (n = 3 mice per genotype) using the Amplex™ Red assay. No significant genotype-dependent differences in cholesterol abundance were observed in either the forebrain or cerebellum (Fig. S10). We additionally performed filipin staining on brain sections and did not observe any overt differences in cholesterol distribution or intensity between wild-type and knock-in mice (data not shown), suggesting that overall cholesterol homeostasis is preserved despite the pronounced alterations in GSL abundance in the knock-in mouse brain.

Bulk transcriptomics of knock-in mouse brain reveals altered expression of genes involved in GSL and sialic acid metabolism

Transcriptomic analyses of mouse forebrain and cerebellum (Cohort IV; n = 4 mice per genotype) showed significantly elevated expression of *Neu1*, which encodes the lysosomal Neu1 sialidase (Miyagi and Yamaguchi, 2012; Monti et al., 2010) (Fig. 4). In the cerebellum, there was also a significant increase in the expression of *Hexa* and *Hexb* (Fig. 4B), which encode the α and β subunits of β-hexosaminidase, respectively. In contrast, expression of *Smpd1*, which encodes acid sphingomyelinase, was significantly reduced in the cerebellum of knock-in mice (Fig. 4B).

We also examined the expression of genes involved in GSL biosynthesis. *St6galnac3*, which encodes a sialyltransferase responsible for catalyzing the biosynthesis of ganglioside GD1α from GM1b (Lee et al., 1999), was significantly reduced in both the forebrain and cerebellum (Figs. 4C and 4D). Additionally, *St3gal3*, a ganglioside biosynthetic enzyme (Schnaar, 2014), exhibited elevated expression in the forebrain but was significantly reduced in the cerebellum of knock-in mice (Figs. 4C and 4D). Notably,

GlcCer synthase (*Ugcg*) expression was not altered in the forebrain or cerebellum of knock-in mice (Supplementary Table 2). Taken together, these findings suggest region-specific alterations in the expression of genes involved in GSL biosynthesis and catabolism. The full dataset of GSL and sialic acid metabolism gene expression results is available in Supplementary Table 2.

Enzyme activity assays validate transcriptomic dysregulation of several glycohydrolases

We next examined lysosomal glycohydrolase activities to determine whether the observed transcriptomic alterations were mirrored at the enzymatic level. Using fluorescent 4-methylumbelliferone (4-MU) assays, we quantified the activities of GSL glycosidases in Cohort I (n = 3 mice per genotype). Specifically, we assessed neuraminidase activity (Neu1/3/4 and Neu2), β-hexosaminidase activity (total Hex and HexA), as well as the activities of glucocerebrosidase (Gba1 and Gba2), α-glucosidase, α-galactosidase, β-galactosidase, and α-mannosidase.

Quantification of Neu1/3/4 and cytosolic Neu2 activities demonstrated a significant increase in Neu1/3/4 activity in the cerebellum, liver, and kidney of knock-in mice, with an upward trend in the forebrain (Figs. 5 and 6). In contrast, Neu2 activity remained unchanged across all examined tissues (Figs. 5 and 6). We next performed two 4-MU assays to quantify β-hexosaminidase activity, measuring both total Hex and HexA. Total Hex activity was elevated in all examined tissues except the kidney, while HexA activity showed significant increases across all tissues (Figs. 5 and 6).

In assaying glucocerebrosidase activity, Gba1 activity was significantly elevated in the forebrain and exhibited an upward trend in the cerebellum, while no significant changes were detected in peripheral tissues (Figs. 5 and 6). In contrast, non-lysosomal Gba2 activity remained unchanged across all examined tissues (Figs. 5 and 6).

We also assessed several additional lysosomal hydrolases. In the forebrain, the activities of α-glucosidase,

α-galactosidase, β-galactosidase, and α-mannosidase were significantly elevated (Fig. 5A). In the cerebellum, all these enzymes were markedly increased, although α-mannosidase showed only a trending elevation (Fig. 5B). In peripheral tissues, α-galactosidase, β-galactosidase, and α-mannosidase activities were elevated in the liver, whereas only α-galactosidase and α-mannosidase were increased in the kidney (Figs. 6A and 6B). Together, these findings highlight tissue-specific enzymatic adaptations to GSL dysregulation in the knock-in model. A summary of these alterations is presented in Fig. 7B.

Discussion and Limitations

This study provides a comprehensive *in vivo* biochemical characterization of GSL metabolism in a FSASD knock-in mouse model. Across all multi-omic modalities, we observed GM2/GA1 accumulation, reduced GlcCer, brain region-specific transcriptional shifts, and selective enzyme activity alterations. Collectively, these results suggest that SLC17A5 deficiency disrupts GSL catabolism in a region-specific manner, representing changes that may both contribute to and arise from neurodegeneration.

Cerebellum as a metabolic hotspot of vulnerability in FSASD

Distinct alterations in GSL metabolism were observed between the forebrain and cerebellum of Slc17a5-R39C/R39C mice compared to wild-type mice, with the cerebellum showing the most prominent changes across nearly all study arms, suggesting a potential role for cerebellar GSL dysregulation in the disease phenotype. Specifically, in the cerebellum, compared to the forebrain, we observed more pronounced alterations in: 1) free and total sialic acid levels, 2) lipid profiles via exploratory untargeted lipidomic analyses, 3) GSL accumulation, and 4) transcriptional changes in genes associated with GSL catabolism. Cerebellar vulnerability aligns with the clinical manifestation of ataxia in FSASD and other lysosomal storage diseases (Walkley et al., 2010), and with imaging evidence of cerebellar white matter involvement (Linnankivi et al., 2003; Varho et al., 2002). Prior studies in the *Slc17a5* knock-out model, which demonstrated CNS myelin deficiency and highlighted the vulnerability of Purkinje cells to lysosomal dysfunction and early degeneration (Walkley et al., 2010), suggest that Purkinje cells may play a role in

the pathogenesis of FSASD. Moreover, Purkinje cell-specific *Ugcg* deletion, the gene that encodes the enzyme responsible for GlcCer synthesis, leads to axonal degeneration and detached paranodal loops, indicating a role for GlcCer-based GSLs in maintaining axonal-myelin integrity (Watanabe et al., 2010). Collectively, our findings, together with prior studies, underscore the need for cell-type-resolved analyses (e.g., Purkinje cells, oligodendrocytes, microglia) in this FSASD knock-in mouse model.

Mechanistic insights into compensatory responses

In our studies, pronounced alterations in GSL levels were observed at the latest timepoints, prompting the question of whether these changes are a direct consequence of the primary defect (SLC17A5 deficiency/impaired sialic acid recycling) or secondary to neurodegenerative processes and selective neural cell loss. Notably, the absence of transcriptional changes in *Ugcg*, together with broadly increased catabolic enzyme activities, suggests that the dysregulation observed in the knock-in mouse brain arises from impaired catabolism rather than altered GSL biosynthesis.

Although β-hexosaminidase activity was elevated in both forebrain and cerebellum, and *Hexa* and *Hexb* expression was upregulated in the cerebellum, GM2 levels remained elevated across cohorts and timepoints, indicating that these compensatory mechanisms are insufficient to fully clear GM2, an intermediate in lysosomal ganglioside catabolism. Moreover, elevated GA2 levels in the knock-in mouse brain (Figs. S4B, S6, and S7) may partially reflect increased conversion of GM2 to GA2. Both humans and mice degrade GM2 via a β-hexosaminidase A-mediated pathway, but mice additionally possess a Neu3 sialidase/β-hexosaminidase B-dependent bypass pathway that additionally facilitates conversion of GM2 into GA2 (Seyrantepe et al., 2018). The presence of the Neu3/HexB-mediated GM2 bypass pathway in mice prevents detectable neurological symptoms in mouse models of Tay-Sachs disease (*Hexa* deficient), whereas Sandhoff mice (*Hexb* deficient) develop progressive neurologic disease (Sango et al., 1995). Broadly, although no substrate reduction therapies are currently approved for GM2 gangliosidosis (Cachon-Gonzalez et al., 2018; Marshall et al., 2019), such approaches have shown promise in preclinical

studies and may represent a potential therapeutic strategy for FSASD.

Notably, in addition to enhanced catabolic flux, elevated GA2 may also arise from altered ganglioside biosynthesis. Impaired availability of activated sialic acid could limit St3gal5-mediated conversion of LacCer to GM3, thereby expanding the LacCer pool available as a substrate for the asialo-GSL pathways. Under these conditions, LacCer could be converted to GA2 and GA1 via B4galnt1 and B3galt4, respectively.

In the forebrain and cerebellum, GlcCer levels were consistently reduced in the knock-in model, accompanied by increased lysosomal Gba1 activity, while cytosolic Gba2 activity remained unchanged. Elevated Gba1 activity facilitates increased lysosomal GlcCer hydrolysis; however, lysosomal glucocerebrosidase is generally not rate-limiting for basal GSL turnover under physiological conditions. Accordingly, the observed reduction in GlcCer abundance is unlikely to be explained solely by enhanced lysosomal degradation. Reduced GlcCer levels may also reflect altered metabolic flux through the GSL pathway, redistribution of GlcCer among subcellular pools, or diversion of GlcCer into alternative biosynthetic or catabolic routes in the context of sialin deficiency. Discriminating among these possibilities requires direct quantification of downstream metabolites, such as glucosylsphingosine (GlcSph), as well as stable-isotope flux-based and subcellular analyses. Nonetheless, these findings support the notion that selective bottlenecks and maladaptive feedback within GSL pathways likely contribute to the pathobiology of FSASD.

Free sialic acid and GSL accumulation

The observed correlation between elevated free sialic acid and increased GSL levels in the knock-in mouse model of FSASD may initially appear paradoxical, given the impaired lysosomal sialic acid recycling characteristic of the disorder. However, the accumulation of free sialic acid within the lysosomes could contribute to secondary GSL storage as free sialic acid can competitively inhibit

lysosomal sialidases (Mendla and Cantz, 1984; Miyagi and Yamaguchi, 2012). Additionally, alterations in the intra-lysosomal environment, such as changes in pH (Schmid et al., 1999) potentially due to sialin deficiency and the accumulation of free sialic acid, may impair multiple acid hydrolases (Pillay et al., 2002).

Although no therapies are currently approved for FSASD, approaches such as GM2 substrate reduction, modulation of sialidase activity, and enhancement of lysosomal function or autophagic flux (e.g., via TFEB activation) are conceptually aligned with our findings. Given the non-uniform regional biology observed in the knock-in mouse brain and human-mouse species-specific differences in GSL metabolism, careful preclinical evaluation will be required to determine appropriate targets and optimal dosing windows.

Limitations

While this study provides valuable insights into the neuropathology of FSASD, several limitations must be acknowledged. First, most experiments were conducted using Cohort I (comprising 1 male and 5 female mice), while Cohorts II-IV consisted exclusively of male mice. This approach was implemented to initially validate the findings from Cohort I and to control for sex as a biological variable, thereby ensuring more streamlined interpretation of the results. Next, enzyme activity and sialic acid levels were not assessed in Cohort III, which precludes an evaluation of early mouse timepoints and effects specifically in male mice. Additionally, this study was performed using a hybrid B6J:S129 mouse background; therefore, consideration should be given to backcrossing the model onto a pure B6J background for future studies to assess background-specific effects. Finally, because the untargeted lipidomics analyses were conducted with a limited number of biological replicates (n = 2 per genotype), additional replicates will be necessary in future studies to enable more robust quantitative conclusions.

Despite these limitations, this study provides a comprehensive biochemical profiling of an *in vivo* mouse model of FSASD, with a focus on the dysregulation of GSL metabolism in the context of the disorder.

The observed dysfunction in the brain highlights the organ's susceptibility and suggests that it plays a role in the neuropathology of FSASD, potentially serving as a target for therapeutic interventions aimed at modulating GSL metabolism or enhancing autophagic flux. Overall, this study underscores the intricate interactions between sialin deficiency and GSL metabolism in neurodegeneration and their potential contribution to FSASD pathogenesis.

Acknowledgements

We acknowledge the NHGRI Mouse Transgenic Core for their assistance in generating the mice used in this study. We are grateful to Carla Ciccone (NIH/NHGRI) for her assistance with sample shipments. We also thank the following Platt laboratory members at the University of Oxford for their collegial guidance: Danielle Te Vruchte (GSLs), David Priestman (GSLs), Reuben Bush (GSLs), and Qiaochu Zhang (enzyme assays). We further thank members of the FSASD Consortium (https://www.star-foundation.io/research-consortium) for their feedback throughout the duration of this study.

Authors' contributions

Conceptualization: MSS, FMP, MCVM

Investigation: MSS, MSH, LP, PL, MCVM

Formal analysis: MSS

Visualization: MSS

Writing - Original Draft: MSS

Writing - Review & Editing: MSS, MSH, LP, PL, MH, WAG, FMP, MCVM

Supervision: MH, WAG, FMP, MCVM

Resources: WAG, FMP, MCVM

Funding acquisition: LP, WAG, FMP

Competing interest statement

The authors declare no conflicts of interest.

Funding

This work was supported in part by the National Institutes of Health (NIH) Intramural Research Program of the National Human Genome Research Institute and other institutes contributing to the NIH Undiagnosed Diseases Program. The contributions of the NIH authors are considered works of the U.S. government. The findings and conclusions presented in this paper are those of the authors and do not necessarily reflect the views of the NIH or the U.S. Department of Health and Human Services. MSS received a graduate fellowship from the National Institutes of Health Oxford-Cambridge Scholars Program. Partial support to MSH was provided by a donation from the Salla Treatment and Research Foundation (STAR) and from the NIH Undergraduate Scholarship Program. The STAR foundation also awarded a grant to Greenwood Genetic Center (LP) for sialic acid quantification.

Ethics statement

Animal care, procedures, and euthanasia were conducted in accordance with the guidelines set forth by the Institutional Animal Care and Use Committee of the NIH National Human Genome Research Institute, under the animal study protocol, G-14-5 (Mouse Models for Disorders of Sialylation).

Data sharing

The datasets generated and analyzed during the current study are available from the corresponding author upon reasonable request. The R scripts used for statistical and visualization analyses have been deposited on GitHub at https://github.com/mssabir/Untargeted-lipidomics-Mousebrain (untargeted lipidomic analyses) and https://github.com/mssabir/BulkRNASeq_MouseBrain_GSLandSAMetabolismPathways (transcriptomic analyses).

References

Adams, D., Wasserstein, M., 2020. Free Sialic Acid Storage Disorders, in: Adam, M.P., Feldman, J., Mirzaa, G.M., Pagon, R.A., Wallace, S.E., Bean, L.J.H., Gripp, K.W., Amemiya, A. (Eds.), GeneReviews((R)), Seattle (WA).

Aula, N., Salomaki, P., Timonen, R., Verheijen, F., Mancini, G., Mansson, J.E., Aula, P., Peltonen, L., 2000. The spectrum of SLC17A5-gene mutations resulting in free sialic acid-storage diseases indicates some genotype-phenotype correlation. Am J Hum Genet 67, 832–840.

Aula, P., Autio, S., Raivio, K.O., Rapola, J., Thoden, C.J., Koskela, S.L., Yamashina, I., 1979. "Salla disease": a new lysosomal storage disorder. Arch Neurol 36, 88–94.

Barmherzig, R., Bullivant, G., Cordeiro, D., Sinasac, D.S., Blaser, S., Mercimek-Mahmutoglu, S., 2017. A New Patient With Intermediate Severe Salla Disease With Hypomyelination: A Literature Review for Salla Disease. Pediatr Neurol 74, 87–91 e82.

Blighe, K.R., S.; Lewis, M., 2018. EnhancedVolcano: Publication-ready volcano plots with enhanced colouring and labeling.

Blom, H.J., Andersson, H.C., Seppala, R., Tietze, F., Gahl, W.A., 1990. Defective glucuronic acid transport from lysosomes of infantile free sialic acid storage disease fibroblasts. Biochem J 268, 621–625.

Cachon-Gonzalez, M.B., Zaccariotto, E., Cox, T.M., 2018. Genetics and Therapies for GM2 Gangliosidosis. Curr Gene Ther 18, 68–89.

Chigorno, V., Tettamanti, G., Sonnino, S., 1996. Metabolic processing of gangliosides by normal and Salla human fibroblasts in culture. A study performed by administering radioactive GM3 ganglioside. J Biol Chem 271, 21738–21744.

Courville, P., Quick, M., Reimer, R.J., 2010. Structure-function studies of the SLC17 transporter sialin identify crucial residues and substrate-induced conformational changes. J Biol Chem 285, 19316–19323.

Davies, L.R., Varki, A., 2015. Why Is N-Glycolylneuraminic Acid Rare in the Vertebrate Brain? Top Curr Chem 366, 31–54.

Dieterle, F., Ross, A., Schlotterbeck, G., Senn, H., 2006. Probabilistic quotient normalization as robust method to account for dilution of complex biological mixtures. Application in 1H NMR metabonomics. Anal Chem 78, 4281–4290.

Gilormini, P.A., Lion, C., Vicogne, D., Levade, T., Potelle, S., Mariller, C., Guerardel, Y., Biot, C., Foulquier, F., 2016. A sequential bioorthogonal dual strategy: ManNAl and SiaNAl as distinct tools to unravel sialic acid metabolic pathways. Chem Commun (Camb) 52, 2318–2321.

Haataja, L., Parkkola, R., Sonninen, P., Vanhanen, S.L., Schleutker, J., Aarimaa, T., Turpeinen, U., Renlund, M., Aula, P., 1994. Phenotypic variation and magnetic resonance imaging (MRI) in Salla disease, a free sialic acid storage disorder. Neuropediatrics 25, 238–244.

Huebecker, M., Moloney, E.B., van der Spoel, A.C., Priestman, D.A., Isacson, O., Hallett, P.J., Platt, F.M., 2019. Reduced sphingolipid hydrolase activities, substrate accumulation and ganglioside decline in Parkinson's disease. Mol Neurodegener 14, 40.

Huizing, M., Hackbarth, M.E., Adams, D.R., Wasserstein, M., Patterson, M.C., Walkley, S.U., Gahl, W.A., Consortium, F., 2021. Free sialic acid storage disorder: Progress and promise. Neurosci Lett 755, 135896.

Kim, D., Paggi, J.M., Park, C., Bennett, C., Salzberg, S.L., 2019. Graph-based genome alignment and genotyping with HISAT2 and HISAT-genotype. Nat Biotechnol 37, 907–915.

Kleta, R., Morse, R.P., Orvisky, E., Krasnewich, D., Alroy, J., Ucci, A.A., Bernardini, I., Wenger, D.A., Gahl, W.A., 2004. Clinical, biochemical, and molecular diagnosis of a free sialic acid storage disease patient of moderate severity. Mol Genet Metab 82, 137–143.

Lee, Y.C., Kaufmann, M., Kitazume-Kawaguchi, S., Kono, M., Takashima, S., Kurosawa, N., Liu, H., Pircher, H., Tsuji, S., 1999. Molecular cloning and functional expression of two members of mouse NeuAcalpha2,3Galbeta1,3GalNAc GalNAcalpha2,6-sialyltransferase family, ST6GalNAc III and IV. J Biol Chem 274, 11958–11967.

Lin, W.-J., Shen, P.-C., Liu, H.-C., Cho, Y.-C., Hsu, M.-K., Lin, I.C., Chen, F.-H., Yang, J.-C., Ma, W.-L., Cheng, W.-C., 2021. LipidSig: a web-based tool for lipidomic data analysis. Nucleic Acids Research 49, W336–W345.

Linnankivi, T., Lonnqvist, T., Autti, T., 2003. A case of Salla disease with involvement of the cerebellar white matter. Neuroradiology 45, 107–109.

Love, M.I., Huber, W., Anders, S., 2014. Moderated estimation of fold change and dispersion for RNA-seq data with DESeq2. Genome Biol 15, 550.

Mancini, G.M., Beerens, C.E., Aula, P.P., Verheijen, F.W., 1991. Sialic acid storage diseases. A multiple lysosomal transport defect for acidic monosaccharides. J Clin Invest 87, 1329–1335.

Marshall, J., Nietupski, J.B., Park, H., Cao, J., Bangari, D.S., Silvescu, C., Wilper, T., Randall, K., Tietz, D., Wang, B., Ying, X., Leonard, J.P., Cheng, S.H., 2019. Substrate Reduction Therapy for Sandhoff Disease through Inhibition of Glucosylceramide Synthase Activity. Mol Ther 27, 1495–1506.

Mendla, K., Cantz, M., 1984. Specificity studies on the oligosaccharide neuraminidase of human fibroblasts. Biochem J 218, 625–628.

Miyagi, T., Yamaguchi, K., 2012. Mammalian sialidases: physiological and pathological roles in cellular functions. Glycobiology 22, 880–896.

Mohamed, A., Molendijk, J., Hill, M.M., 2020. lipidr: A Software Tool for Data Mining and Analysis of Lipidomics Datasets. J Proteome Res 19, 2890–2897.

Monti, E., Bonten, E., D'Azzo, A., Bresciani, R., Venerando, B., Borsani, G., Schauer, R., Tettamanti, G., 2010. Sialidases in vertebrates: a family of enzymes tailored for several cell functions. Adv Carbohydr Chem Biochem 64, 403–479.

Morin, P., Sagne, C., Gasnier, B., 2004. Functional characterization of wild-type and mutant human sialin. EMBO J 23, 4560–4570.

Morse, R.P., Kleta, R., Alroy, J., Gahl, W.A., 2005. Novel form of intermediate salla disease: clinical and neuroimaging features. J Child Neurol 20, 814–816.

590 Pietrancosta, N., Anne, C., Prescher, H., Ruivo, R., Sagne, C., Debacker, C., Bertrand, H.O., Brossmer,
591 R., Acher, F., Gasnier, B., 2012. Successful prediction of substrate-binding pocket in SLC17 transporter
592 sialin. J Biol Chem 287, 11489–11497.
593 Pillay, C.S., Elliott, E., Dennison, C., 2002. Endolysosomal proteolysis and its regulation. Biochem J 363,
594 417–429.
595 Pitto, M., Chigorno, V., Renlund, M., Tettamanti, G., 1996. Impairment of ganglioside metabolism in
596 cultured fibroblasts from Salla patients. Clin Chim Acta 247, 143–157.
597 Platt, F.M., 2023. The expanding boundaries of sphingolipid lysosomal storage diseases; insights from
598 Niemann-Pick disease type C. Biochem Soc Trans 51, 1777–1787.
599 Priestman, D.A., Sabir, M.S., Bush, R., te Vruchte, D., Wallom, K.L., Fernández-Suárez, M.E., Platt,
600 F.M., 2024. Analysis of glycosphingolipids from animal tissues. protocols.io.
601 Renlund, M., Aula, P., Raivio, K.O., Autio, S., Sainio, K., Rapola, J., Koskela, S.L., 1983. Salla disease: a
602 new lysosomal storage disorder with disturbed sialic acid metabolism. Neurology 33, 57–66.
603 Ridley, C.M., Thur, K.E., Shanahan, J., Thillaiappan, N.B., Shen, A., Uhl, K., Walden, C.M., Rahim,
604 A.A., Waddington, S.N., Platt, F.M., van der Spoel, A.C., 2013. beta-Glucosidase 2 (GBA2) activity and
605 imino sugar pharmacology. J Biol Chem 288, 26052–26066.
606 Rosner, H., 2003. Developmental expression and possible roles of gangliosides in brain development.
607 Prog Mol Subcell Biol 32, 49–73.
608 Sabir, M.S., Hackbarth, M.E., Burke, J.D., Garrett, L.J., Elliott, G., Rivas, C., Springer, D.A., Leoyklang,
609 P., Clark, T.S., Huizing, M., Gahl, W.A., Malicdan, M.C.V., 2022. A novel experimental mouse model to
610 investigate a free sialic acid storage disorder (Salla disease). Mol Genet Metab 135, S107.
611 Sabir, M.S., Jovanovic, V.M., Ryu, S., Sen, C., Ormanoglu, P., Pollard, L., Steet, R., Gahl, W.A.,
612 Huizing, M., Tristan, C.A., Platt, F.M., Malicdan, M.C.V., 2025a. Lysosomal free sialic acid storage
613 disorder iPSC-derived neural cells display altered glycosphingolipid metabolism. Sci Rep 15, 29708.

Sabir, M.S., Wolfe, L., Adams, D.R., Ciccone, C., Porter, F.D., Gahl, W.A., Huizing, M., Platt, F.M., Malicdan, M.C.V., 2025b. Changes in glycosphingolipid levels in plasma and cerebrospinal fluid of individuals with Lysosomal Free Sialic Acid Storage Disorder. Rare 3, 100065.

Saeui, C.T., Nairn, A.V., Galizzi, M., Douville, C., Gowda, P., Park, M., Dharmarha, V., Shah, S.R., Clarke, A., Austin, M., Moremen, K.W., Yarema, K.J., 2018. Integration of genetic and metabolic features related to sialic acid metabolism distinguishes human breast cell subtypes. PLoS One 13, e0195812.

Sagne, C., Gasnier, B., 2008. Molecular physiology and pathophysiology of lysosomal membrane transporters. J Inherit Metab Dis 31, 258–266.

Sango, K., Yamanaka, S., Hoffmann, A., Okuda, Y., Grinberg, A., Westphal, H., McDonald, M.P., Crawley, J.N., Sandhoff, K., Suzuki, K., Proia, R.L., 1995. Mouse models of Tay-Sachs and Sandhoff diseases differ in neurologic phenotype and ganglioside metabolism. Nat Genet 11, 170–176.

Schauer, R., Kamerling, J.P., 2018. Exploration of the Sialic Acid World. Adv Carbohydr Chem Biochem 75, 1–213.

Schmid, J.A., Mach, L., Paschke, E., Glossl, J., 1999. Accumulation of sialic acid in endocytic compartments interferes with the formation of mature lysosomes. Impaired proteolytic processing of cathepsin B in fibroblasts of patients with lysosomal sialic acid storage disease. J Biol Chem 274, 19063–19071.

Schnaar, R.L., 2014. ST3 Beta-Galactoside Alpha-2,3-Sialyltransferase 3 (ST3GAL3), in: Taniguchi, N., Honke, K., Fukuda, M., Narimatsu, H., Yamaguchi, Y., Angata, T. (Eds.), Handbook of Glycosyltransferases and Related Genes. Springer Japan, Tokyo, pp. 657–665.

Schnaar, R.L., Suzuki, A., Stanley, P., 2009. Glycosphingolipids, in: Varki, A., Cummings, R.D., Esko, J.D., Freeze, H.H., Stanley, P., Bertozzi, C.R., Hart, G.W., Etzler, M.E. (Eds.), Essentials of Glycobiology, 2nd ed, Cold Spring Harbor (NY).

Seyrantepe, V., Demir, S.A., Timur, Z.K., Von Gerichten, J., Marsching, C., Erdemli, E., Oztas, E., Takahashi, K., Yamaguchi, K., Ates, N., Donmez Demir, B., Dalkara, T., Erich, K., Hopf, C., Sandhoff,

R., Miyagi, T., 2018. Murine Sialidase Neu3 facilitates GM2 degradation and bypass in mouse model of Tay-Sachs disease. Exp Neurol 299, 26–41.

Simons, K., Ikonen, E., 1997. Functional rafts in cell membranes. Nature 387, 569–572.

Sonninen, P., Autti, T., Varho, T., Hamalainen, M., Raininko, R., 1999. Brain involvement in Salla disease. AJNR Am J Neuroradiol 20, 433–443.

Svennerholm, L., 1980. Gangliosides and synaptic transmission. Adv Exp Med Biol 125, 533–544.

Varho, T.T., Alajoki, L.E., Posti, K.M., Korhonen, T.T., Renlund, M.G., Nyman, S.R., Sillanpaa, M.L., Aula, P.P., 2002. Phenotypic spectrum of Salla disease, a free sialic acid storage disorder. Pediatr Neurol 26, 267–273.

Verheijen, F.W., Verbeek, E., Aula, N., Beerens, C.E., Havelaar, A.C., Joosse, M., Peltonen, L., Aula, P., Galjaard, H., van der Spek, P.J., Mancini, G.M., 1999. A new gene, encoding an anion transporter, is mutated in sialic acid storage diseases. Nat Genet 23, 462–465.

Vyas, A.A., Schnaar, R.L., 2001. Brain gangliosides: functional ligands for myelin stability and the control of nerve regeneration. Biochimie 83, 677–682.

Walkley, S.U., Sikora, J., Micsenyi, M., Davidson, C., Dobrenis, K., 2010. Lysosomal compromise and brain dysfunction: examining the role of neuroaxonal dystrophy. Biochem Soc Trans 38, 1436–1441.

Watanabe, S., Endo, S., Oshima, E., Hoshi, T., Higashi, H., Yamada, K., Tohyama, K., Yamashita, T., Hirabayashi, Y., 2010. Glycosphingolipid synthesis in cerebellar Purkinje neurons: roles in myelin formation and axonal homeostasis. Glia 58, 1197–1207.

Wreden, C.C., Wlizla, M., Reimer, R.J., 2005. Varied mechanisms underlie the free sialic acid storage disorders. J Biol Chem 280, 1408–1416.

Yang, L.J., Zeller, C.B., Shaper, N.L., Kiso, M., Hasegawa, A., Shapiro, R.E., Schnaar, R.L., 1996. Gangliosides are neuronal ligands for myelin-associated glycoprotein. Proc Natl Acad Sci U S A 93, 814–818.

Figure legends

Figure 1. Sialic acid levels across mouse tissues (Cohort I; n = 3 mice per genotype). (A) free sialic acid levels, **(B)** total sialic acid levels, and **(C)** bound sialic acid levels. Bound levels were derived by subtracting free levels from total levels. All levels were normalized to total protein content. Each point corresponds to one biological sample. Mean ± SEM; unpaired t-test with *p*-value <0.05 (*), <0.005 (**), <0.0006 (***), <0.0001 (****), and ns = not significant.

Figure 2. Levels of total GSLs and individual GSL species in mouse forebrain and cerebellum (Cohort I; n = 3 mice per genotype). Levels in **(A)** forebrain and **(B)** cerebellum. Levels were normalized to total protein content. Each point corresponds to one biological sample. Mean ± SEM; unpaired t-test *p*-value <0.05 (*), <0.0099 (**), <0.0001 (***), and ns = not significant.

Figure 3. Levels of total GSLs and individual GSL species in mouse peripheral tissues (Cohort I; n = 3 mice per genotype). Levels in **(A)** liver and **(B)** kidney. Levels were normalized to total protein content. Each point corresponds to one biological sample. Mean ± SEM; unpaired t-test *p*-value <0.05 (*), <0.0001 (***), and ns = not significant.

Figure 4. Glycosphingolipid (GSL) and sialic acid (SA) metabolism gene expression in mouse forebrain and cerebellum (Cohort IV; n = 4 mice per genotype). GSL biosynthesis and catabolism gene expression in **(A)** forebrain and **(B)** cerebellum. SA biosynthesis and catabolism gene expression in **(C)** forebrain and **(D)** cerebellum. Log_2 fold change cut-off set at 0 and adjusted $-log_{10}$ *p*-value cut-off set at $10^{-1.3}$ (0.05). Red circles (with gene names annotated) indicate genes up or down-regulated meeting the indicated *p*-value and log_2 fold-change cut-offs. Green circles indicate genes not significantly altered per the noted *p*-value and log_2 fold-change cut-offs. Refer to Supplementary Table 2 for full details on GSL and SA metabolism gene expression across each brain region.

Figure 5. Activity levels of enzymes involved in GSL catabolism in mouse brain tissues (Cohort I; n = 3 mice per genotype). Activity levels in **(A)** forebrain and **(B)** cerebellum. The following enzyme activities were measured: neuraminidase (Neu1/3/4 and Neu2); β-hexosaminidase (total Hex and HexA); α-glucosidase (α-gluc); glucocerebrosidase (Gba1 and Gba2); α-galactosidase (α-gal); β-galactosidase (β-gal); and α-mannosidase (α-mann), described in (Platt, 2023). Activity represented as nmol per hour per mg total protein content. Each point corresponds to one biological sample. Mean ± SEM; unpaired t-test *p*-value <0.05 (*), <0.009 (**), <0.0009 (***), <0.0001 (****), and ns = not significant.

Figure 6. Activity levels of enzymes involved in GSL catabolism in mouse peripheral tissues (Cohort I; n = 3 mice per genotype). Activity levels in **(A)** liver and **(B)** kidney. The following enzyme activities were measured in each tissue: neuraminidase (Neu1/3/4 and Neu2); β-hexosaminidase (total Hex and HexA); α-glucosidase (α-gluc); glucocerebrosidase (Gba1 and Gba2); α-galactosidase (α-gal); β-galactosidase (β-gal); and α-mannosidase (α-mann). Activity represented as nmol per hour per mg total protein content. Each point corresponds to one mouse. Mean ± SEM; unpaired t-test *p*-value <0.05 (*), <0.005 (**), <0.0008 (***), and ns = not significant.

Figure 7. Summary of GSL and enzyme activity levels across mouse tissues (Cohort I; n = 3 mice per genotype). Summary of **(A)** GSL and **(B)** enzyme activity results in Slc17a5-R39C/R39C versus wild-type mice. Up arrows denote significantly elevated GSL species or enzyme activities, while down arrows indicate significantly reduced levels or activities. An equal sign signifies no significant difference between Slc17a5-R39C/R39C and wild-type mice. NA (not applicable) indicates that the GSL was not detected in the specified mouse tissue.

Supplementary figure legends

Supplementary Figure 1. Normalization, principal component analysis (PCA), and hierarchical clustering in mouse cerebellum, forebrain, and hemisphere (Cohort II; n = 2 mice per genotype). Probabilistic quotient normalization of samples in **(A)** positive ion and **(B)** negative ion. PCA of samples in **(C)** positive ion and **(D)** negative ion. Hierarchical clustering of samples in **(E)** positive ion and **(F)** negative ion. QC, quality control sample; LH, left hemisphere; RC, right cerebellum; RF, right forebrain; WT, wild-type; R39C, Slc17a5-R39C/R39C.

Supplementary Figure 2. Differential lipid abundance and lipid class enrichment in mouse cerebellum, forebrain, and hemisphere (Cohort II; n = 2 mice per genotype). Differential lipid abundance in **(A)** positive ion and **(B)** negative ion. Significance threshold set at 0.05. Log_2 fold change cut-off set at 1. Number of significant lipids noted in each panel. Lipid class enrichment in **(C)** positive ion and **(D)** negative ion. Significance threshold set at 0.05.

Supplementary Figure 3. Lipid class and Reactome pathway enrichment in mouse brain by *Slc17a5* genotype (Cohort II; n = 2 mice per genotype). Lipid class enrichment in **(A)** positive ion and **(B)** negative ion. Significance threshold set at 0.05. Using LipidSig, reactome pathway enrichment using normalized data is shown for **(C)** positive ion (HexCer, LPC, PI, TAG) and **(D)** negative ion (HexCer, Cer) modes, using Fisher's exact test (p-value ≤0.05), top 10 significant terms, and a gene similarity threshold of 0.5. In the positive ion mode, the top three enriched pathways included post-translational protein modification (123 lipids, 191 pathway genes, $-\log_{10}p = 16.11$), post-translational modification: synthesis of GPI-anchored proteins (74 lipids, 81 pathway genes, $-\log_{10}p = 14.41$), and diseases of signal transduction by growth factor receptors and second messengers (5 lipids, 181 pathway genes, $-\log_{10}p = 13.21$). In the negative ion mode, the top three enriched pathways included sphingolipid metabolism (46 lipids, 61 pathway genes, $-\log_{10}p = 21.88$), formation of the cornified envelope (39 lipids, 43 pathway genes, $-\log_{10}p = 20.28$), and keratinization (39 lipids, 43 pathway genes, $-\log_{10}p = 20.28$).

Supplementary Figure 4. GSL levels in mouse tissues (Cohort I; n = 3 mice per genotype). Levels of **(A)** Lac, **(B)** GA2, and **(C)** several GSL species in the kidney tissues are provisionally assigned and require confirmation via serial enzyme digestion and are included here to ensure comprehensive representation. Each point corresponds to one biological sample. Mean ± SEM; unpaired t-test *p*-value <0.002 (**) and ns = not significant.

Supplementary Figure 5. Representative HPLC traces of GSLs and glucosylceramide (GlcCer) assays in mouse tissues (Cohort I; n = 3 mice per genotype). GSL HPLC trace in **(A)** forebrain, **(B)** cerebellum, **(C)** liver, and **(D)** kidney tissue annotated with provisionally assigned GSL species. **(E)** Representative GlcCer HPLC trace from mouse brain (similar for all tissues).

Supplementary Figure 6. Levels of total GSLs and individual GSL species in mouse forebrain across three timepoints (Cohort III; n = 4-5 wild-type and n = 3-6 Slc17a5-R39C/R39C mice). Timepoints include 21-days, ~3 months, and ~5 months. Levels were normalized to total protein content. Each point corresponds to one mouse, one outlier removed from the R39C/R39C group at 21-days. Mean ± SEM; ordinary ANOVA using Šídák's multiple comparisons test *p*-value <0.05 (*), <0.005 (**), <0.0009 (***), <0.0001 (****), and ns = not significant. Statistical analyses were not performed for the ~5-month timepoint due to limited sample size.

Supplementary Figure 7. Levels of total GSLs and individual GSL species in mouse cerebellum across three timepoints (Cohort III; n = 4-5 wild-type and n = 3-6 Slc17a5-R39C/R39C mice). Timepoints include 21-days, ~3 months, and ~5 months. Levels were normalized to total protein content. Each point corresponds to one mouse. Mean ± SEM; ordinary ANOVA using Šídák's multiple comparisons test *p*-value <0.05 (*), <0.005 (**), <0.0005 (***), <0.0001 (****), and ns = not significant. Statistical analyses were not performed for the ~5-month timepoint due to limited sample size.

Supplementary Figure 8. Immunofluorescence studies in male mouse cerebellum and pons. Immunostaining for DAPI (blue), GM2 (green dots), and LAMP1 (red dots) in the cerebellum of **(A)** 91-day-old (n = 1 mouse per genotype) and **(B)** 270-day-old mice (n = 1 mouse per genotype). Similar staining in the pons of **(C)** 91-day-old and **(D)** 270-day-old mice. 20X (100 µm scale bar) unless otherwise noted as 63X (20 µm scale bar). WT, wild-type; R39C/R39C, Slc17a5-R39C/R39C.

Supplementary Figure 9. Quantification of bound sialic acid from GSLs extracted from mouse brains (Cohort I; n = 3 mice per genotype). Bound sialic acid levels in **(A)** forebrain and **(B)** cerebellum. Each point corresponds to one mouse. Mean ± SEM; unpaired t-test *p*-values as indicated.

Supplementary Figure 10. Amplex™ Red quantitation of free cholesterol and cholesteryl esters in mouse brain homogenates (Cohort I; n = 3 mice per genotype). Abundance in **(A)** forebrain and **(B)** cerebellum. Levels were normalized to total protein content. Each point corresponds to one mouse. Mean ± SEM; unpaired t-test *p*-values as indicated.

Tables

Supplementary Table 1. Description of mice included in this study

Supplementary Table 2. Expression of GSL and SA metabolism genes in Slc17a5-R39C/R39C mouse brain (forebrain and cerebellum) relative to wild-type